Numerical Computation of Two-Dimensional Viscous Blunt Body Flows with an Impinging Shock

J. C. Tannehill* and T. L. Holst†
Iowa State University, Ames, Iowa

and

J. V. Rakich‡
NASA Ames Research Center, Moffett Field, Calif.

Two-dimensional, viscous, blunt body flows with an impinging shock wave are computed using a time-dependent, finite-difference method to solve the complete set of Navier-Stokes equations. The bow shock wave is treated as a discontinuity, whereas all interior shock layer detail such as shear layers, shock waves, jets, and the wall boundary layer are captured automatically in the solution. Numerical results are presented for cases in which shock waves of different strengths are allowed to impinge on the flowfield surrounding a circular cylinder, resulting in different shock interference patterns. The two-dimensional results are compared qualitatively with existing three-dimensional experiments.

Nomenclature

c = relative thickness of refined portion of mesh
c_p = specific heat at constant pressure
C_1, C_2 = constants in Sutherland's equation
D = diameter of cylinder
e = specific internal energy
E = total energy, $\rho[e+(u^2+v^2)/2]$
i_η = unit vector in normal direction
i_ξ = unit vector in tangential direction
k = coefficient of thermal conductivity
K = local radius of curvature
M = Mach number
n_s = outward unit normal to bow shock
p = pressure
Pr = Prandtl number $c_p\mu/k$
q_j = heat flux vector
R = gas constant
Re_D = Reynolds number based on diameter
Re_Δ = min $(Re_{\Delta\eta}, Re_{\Delta\xi})$
$Re_{\Delta\eta}$ = $|\rho v\Delta\eta/\mu|$
$Re_{\Delta\xi}$ = $|\rho u\Delta\xi/\mu|$
t = time
$\bar{t}$ = transformed time
u = tangential velocity component
U_s = local shock velocity
v = normal velocity component
V_1 = fluid velocity normal to shock
y,z = transformed coordinates given by Eq. (14)
$\bar{y},\bar{z}$ = transformed coordinates given by Eq. (13)
α = transformation parameter
β = stretching factor
γ = specific heat ratio
δ = local distance between body and shock
δ_y = $\partial\delta/\partial y$
δ_t = $\partial\delta/\partial t$
δ_ξ = $\partial\delta/\partial\xi$
η = coordinate measured normal to body
θ = angle measured from stagnation streamline
μ = viscosity coefficient
ξ = coordinate measured along body
ρ = density
τ_{ij} = shear stress tensor

Subscripts and superscripts

j = mesh point location in z direction
k = mesh point location in y direction
stag = stagnation point value without impingement
w = wall value
∞ = freestream value
n = time step location

Introduction

An extraneous shock wave impinging on a blunt body in a hypersonic flow has been observed to greatly increase both the heat-transfer rate and pressure near the impingement point. In fact, Hains and Keyes[1] have measured peak heating rates up to 17 times the ordinary stagnation point rate and pressure peaks up to 8 times the freestream pitot pressure as a result of shock impingement. Flowfields of this type may occur on the space shuttle and other maneuverable re-entry vehicles.

The intense heating and high pressures occur over a small region where a disturbance, originating at the intersection of the impinging shock and bow shock, strikes the body. The disturbance may be a free shear layer, a supersonic jet, or a shock wave, depending on the strength and location of the impinging shock and the shape of the body. Edney[2] has described six different types of shock interference patterns which can occur. If the impinging shock wave strikes the bow shock in the region where the shock layer is subsonic, either a Type III or a Type IV interference pattern will result. These interference patterns are shown in Fig. 1. In the Type III interference pattern, the disturbance is a shear layer that attaches to the surface of the body. In the Type IV interference pattern, the disturbance is a supersonic jet that is embedded in the subsonic portion of the flowfield. This latter interference pattern will produce the greatest heating rates and pressures.

Presented as Paper 75-154 at the AIAA 13th Aerospace Sciences Meeting, Pasadena, Calif., January 20-22, 1975; submitted February 20, 1975; revision received July 21, 1975. This work was supported by NASA Ames Research Center under Grant NGR 16-002-038 and the Engineering Research Institute, Iowa State University, Ames, Iowa.

Index category: Supersonic and Hypersonic Flow.

*Associate Professor, Department of Aerospace Engineering and Engineering Research Institute. Member AIAA.

†Research Associate, Department of Aerospace Engineering and Engineering Research Institute; now Aerospace Engineer, Analytical Fluid Mechanics Section, High-Speed Aerodynamics Division, NASA Langley Research Center. Member AIAA.

‡Research Scientist. Associate Fellow AIAA.

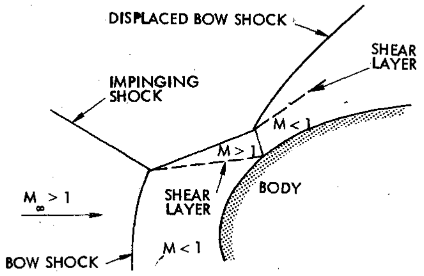

TYPE III

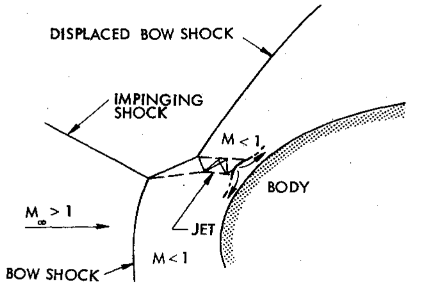

TYPE IV

Fig. 1 Type III and Type IV shock interference patterns.

Because of the very complicated nature of shock impingement flowfields, previous attempts[2-5] at predicting the maximum heating rates and pressures have been limited to semiempirical approaches. Parameters such as the angle between the impinging shock and the bow shock and the bow shock standoff distance (after impingement) must be specified somehow before these methods can be employed. This empiricism has been eliminated for the first time during the present study by numerically computing the entire shock impingement flowfield. This was accomplished by using a "time-dependent," finite-difference method to solve the complete set of Navier-Stokes equations for a compressible, laminar flow. The major reason for using the "time-dependent" method is that the resulting unsteady Navier-Stokes equations are a mixed set of hyperbolic-parabolic equations for both subsonic and supersonic flows. As a result, a very complicated flowfield, such as one of those shown in Fig. 1 where both subsonic and supersonic regions are present, can be calculated as an initial-value problem. An additional advantage is that, since the complete Navier-Stokes equations are solved, all shock waves, shear layers, jets, and the wall boundary layer are "captured" automatically in the solution without prior knowledge of their location or even existence.

For very low Reynolds number flows, the entire shock impingement flowfield, including the bow shock, can be "captured" using this so-called "shock-capturing" approach. This approach was used for computations made during the early stages of the present study.[6] However, it was found that for higher Reynolds number flows it was not practical to "capture" the bow shock because of the numerical difficulties associated with the large gradients at the bow shock. Instead, it was found to be more convenient to treat the bow shock as a discontinuity, across which the Rankine-Hugoniot equations could be applied, while leaving the boundary layer and interaction regions to be captured as before. This latter approach is the so-called "shock-fitting" method.

The numerical methods and results described in this paper are strictly two-dimensional. Unfortunately, most experimental studies have been inherently three-dimensional, being generated by a planar shock impinging on an axisymmetric body. These three-dimensional flowfields do have a plane of symmetry, however, in which the flow is qualitatively the same as in a corresponding two-dimensional flowfield. In the present paper, qualitative comparisons are made in this manner to give credibility to the computed two-dimensional results.

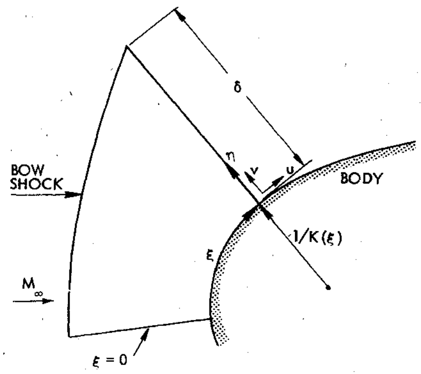

Fig. 2 Two-dimensional body intrinsic coordinate system.

Governing Equations

The fundamental governing equations for an unsteady flow without body forces or external heat additions can be written in conservation-law form for a two-dimensional, body intrinsic coordinate system (see Fig. 2) as

$$\partial\bar{U}/\partial t+\partial\bar{F}/\partial\xi+\partial\bar{G}/\partial\eta+\bar{H}=0 \tag{1}$$

where

$$\bar{U}=(1+K\eta)\begin{bmatrix}\rho\\ \rho u\\ \rho v\\ E\end{bmatrix} \tag{2}$$

$$\bar{F}=\begin{bmatrix}\rho u\\ p+\rho u^2-\tau_{\xi\xi}\\ \rho uv-\tau_{\xi\eta}\\ Eu+pu+q_\xi-u\tau_{\xi\xi}-v\tau_{\xi\eta}\end{bmatrix} \tag{3}$$

$$\bar{G}=(1+K\eta)\begin{bmatrix}\rho v\\ \rho uv-\tau_{\eta\xi}\\ p+\rho v^2-\tau_{\eta\eta}\\ Ev+pv+q_\eta-u\tau_{\eta\xi}-v\tau_{\eta\eta}\end{bmatrix} \tag{4}$$

$$\bar{H}=\begin{bmatrix}0\\ K(\rho uv-\tau_{\xi\eta})\\ -K(p+\rho u^2-\tau_{\xi\xi})\\ 0\end{bmatrix} \tag{5}$$

In addition to the preceding conservation equations, an equation of state in the form

$$p=p(e,\rho) \tag{6}$$

must be specified. For a perfect gas, this equation can be written as

$$p=(\gamma-1)\rho e \tag{7}$$

For the case of air in chemical equilibrium, approximate curve fits are available for Eq. (6) in Refs. 7 and 8.

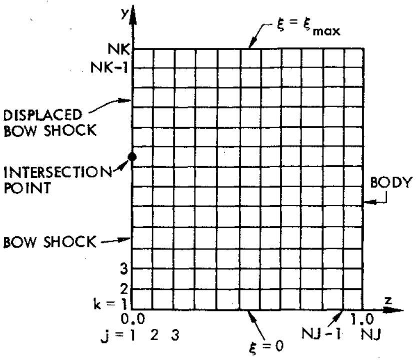

Fig. 3 **Computational plane.**

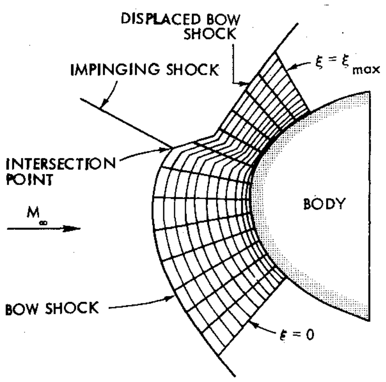

Fig. 4 Physical plane ($\alpha=0$).

The Navier-Stokes expressions for the components of the shearing stress tensor and the heat flux vector are

$$\tau_{\xi\xi}=\mu\, e_{\xi\xi}-\tfrac{1}{3}\mu(e_{\xi\xi}+e_{\eta\eta}) \tag{8a}$$

$$\tau_{\eta\eta}=\mu\, e_{\eta\eta}-\tfrac{1}{3}\mu(e_{\xi\xi}+e_{\eta\eta}) \tag{8b}$$

$$\tau_{\xi\eta}=\tau_{\eta\xi}=\mu e_{\xi\eta} \tag{8c}$$

where

$$e_{\xi\xi}=\frac{2}{1+K\eta}\left[\frac{\partial u}{\partial \xi}+Kv\right] \tag{9a}$$

$$e_{\eta\eta}=2(\partial v/\partial\eta) \tag{9b}$$

$$e_{\xi\eta}=\left[\frac{1}{1+K\eta}\right]\left[\frac{\partial v}{\partial\xi}\right]+\frac{\partial u}{\partial\eta}-\left[\frac{Ku}{1+K\eta}\right] \tag{9c}$$

and

$$q_{\xi}=\frac{-k}{1+K\eta}\frac{\partial T}{\partial\xi},\quad q_{\eta}=-k\frac{\partial T}{\partial\eta} \tag{10}$$

To complete the system of equations, it is necessary to specify expressions for the viscosity (μ) and the coefficient of thermal conductivity (k). For the present study, Sutherland's equation

$$\mu=C_1T^{3/2}/(T+C_2) \tag{11}$$

is used to determine the viscosity, and the coefficient of thermal conductivity is computed by assuming a constant Prandtl number:

$$k=\gamma R\mu/(\gamma-1)Pr \tag{12}$$

Two independent variable transformations are applied to the governing equations just listed. The first transformation maps the computational domain into a rectangular region in the transformed ($\bar{y}$, $\bar{z}$) plane. The equations fo the first independent variable transformation are

$$\bar{y}=\xi,\quad \bar{z}=1-(\eta/\delta),\quad \bar{t}=t \tag{13}$$

where $\delta(\xi,t)$ is the local distance between the body and the shock.

The second independent variable transformation, similar to one introduced in Ref. 9, stretches the computational mesh in the direction normal to the body. The equations for this transformation are

$$y=\bar{y},\ z=\alpha+(1-\alpha)\frac{\ln\left[\dfrac{\beta+\bar{z}(2\alpha+1)-2\alpha}{\beta-\bar{z}(2\alpha+1)+2\alpha}\right]}{\ln\left[\dfrac{\beta+1}{\beta-1}\right]},\ t=\bar{t} \tag{14}$$

where β is related to the approximate boundary-layer thickness (c) by

$$\beta=(1-c)^{-1/2}\qquad(0<c<1) \tag{15}$$

This transformation permits the mesh to be either refined near the body ($\alpha=0$) or refined equally near both the body and the bow shock ($\alpha=\tfrac{1}{2}$). By refining the mesh near the body, it is possible to describe the boundary layer more accurately. On the other hand, it may be desirable to refine the mesh at both the body and the bow shock for shock impingement computations.

After employing the two transformations given by Eqs. (13) and (14), the final computational grid in the (y, z) plane is shown in Fig. 3, and the corresponding grid in the physical plane (ξ,η) is shown in Fig. 4 for $\alpha=0$.

The final forms of the conservation equations are

$$\partial \boldsymbol{U}/\partial t+\partial \boldsymbol{F}/\partial y+\partial \boldsymbol{G}/\partial z+\boldsymbol{H}=0 \tag{16}$$

where

$$\boldsymbol{U}=\delta\bar{\boldsymbol{U}},\quad \boldsymbol{F}=\delta\bar{\boldsymbol{F}} \tag{17a}$$

$$\boldsymbol{G}=(\partial z/\partial\bar{z})\left[(1-\bar{z})(\delta_t\bar{\boldsymbol{U}}+\delta_y\bar{\boldsymbol{F}})-\bar{\boldsymbol{G}}\right] \tag{17b}$$

$$\begin{aligned}\boldsymbol{H}=\delta\bar{\boldsymbol{H}}-\boldsymbol{G}\{&\ln\left[(\beta+1)/(\beta-1)\right]\ [\bar{z}(2\alpha+1)\\&-2\alpha]/[\beta(1-\alpha)]\}\end{aligned} \tag{17c}$$

The transformed expressions for the components of the shearing stress tensor and heat flux vector are

$$\begin{aligned}e_{\xi\xi}=&\left[\frac{2}{1+K\delta(1-\bar{z})}\right]\left[\frac{\partial u}{\partial y}\right.\\&\left.+(1-\bar{z})\frac{\delta_y}{\delta}\frac{\partial z}{\partial\bar{z}}\frac{\partial u}{\partial z}+Kv\right]\end{aligned} \tag{18a}$$

$$e_{\eta\eta}=-\frac{2}{\delta}\frac{\partial z}{\partial\bar{z}}\frac{\partial v}{\partial z} \tag{18b}$$

$$\begin{aligned}e_{\xi\eta}=&\left[\frac{1}{1+K(1-\bar{z})\delta}\right]\left[\frac{\partial v}{\partial y}+(1-\bar{z})\frac{\delta_y}{\delta}\frac{\partial z}{\partial\bar{z}}\frac{\partial v}{\partial z}\right]\\&-\frac{1}{\delta}\frac{\partial z}{\partial\bar{z}}\frac{\partial u}{\partial z}-\frac{Ku}{1+K(1-\bar{z})\delta}\end{aligned} \tag{18c}$$

$$q_{\xi}=\left[\frac{-k}{1+K(1-\bar{z})\delta}\right]\left[\frac{\partial T}{\partial y}+(1-\bar{z})\frac{\delta_y}{\delta}\frac{\partial z}{\partial\bar{z}}\frac{\partial T}{\partial z}\right] \tag{19a}$$

$$q_{\eta}=\frac{k}{\delta}\frac{\partial z}{\partial\bar{z}}\frac{\partial T}{\partial z} \tag{19b}$$

where

$$\bar{z}=\frac{(\beta+2\alpha)\,[\,(\beta+1)/(\beta-1)\,]^{(z-\alpha)/(1-\alpha)}-\beta+2\alpha}{(2\alpha+1)\{1+[\,(\beta+1)/(\beta-1)\,]^{(z-\alpha)/(1-\alpha)}\}} \tag{20a}$$

$$\frac{\partial z}{\partial \bar{z}}=\frac{2\beta(1-\alpha)(2\alpha+1)}{\{\beta^2-[\bar{z}(2\alpha+1)-2\alpha]^2\}\ln[(\beta+1)/(\beta-1)]} \tag{20b}$$

Numerical Solution of Equations

Finite-Difference Scheme

MacCormack's finite-difference scheme[10] is used to solve the governing equations at each interior grid point. This explicit scheme has second-order accuracy in both space and time. When MacCormack's algorithm is applied to Eq.(16), the following predictor-corrector equations result:

$$\overline{U^{n+1}_{j,k}}=U^n_{j,k}-\frac{\Delta t}{\Delta y}\,(F^n_{j,k+1}-F^n_{j,k})-\frac{\Delta t}{\Delta z}\,(G^n_{j+1,k}-G^n_{j,k})-\Delta t\,H^n_{j,k} \tag{21}$$

$$U^{n+1}_{j,k}=\tfrac{1}{2}\Big[\,U^n_{j,k}+\overline{U^{n+1}_{j,k}}-\frac{\Delta t}{\Delta y}\,(\overline{F^{n+1}_{j,k}}-\overline{F^{n+1}_{j,k-1}})-\frac{\Delta t}{\Delta z}\,(\overline{G^{n+1}_{j,k}}-\overline{G^{n+1}_{j-1,k}})-\Delta t\,\overline{H^{n+1}_{j,k}}\,\Big] \tag{22}$$

where $z=j\Delta z,\ \ y=k\Delta y,\ \ t=n\Delta t,$

and $F^n_{j,k}=F(U^n_{j,k}),\overline{F^{n+1}_{j,k}}=F(\overline{U^{n+1}_{j,k}})$, etc.

Note that the spatial derivatives in the predictor step are approximated by forward differences, whereas in the corrector step they are approximated by backward differences. The shear and heat flux terms appearing in *F*, *G*, and *H* are evaluated using backward differences in the predictor step and forward differences in the corrector step. The net result is a central difference approximation for the shear stress and heat flux terms.[11] Using this finite-difference scheme, the computation is advanced in time from the initial conditions until the "steady-state" solution is reached.

Boundary Conditions

The flow conditions along the leftmost boundary ($j=1$ in Fig. 3) are those conditions that exist immediately downstream of the bow shock as determined by the Rankine-Hugoniot relations. Consequently, it is necessary to permit this boundary to move with the bow shock as the latter moves toward its "steady-state" position. The approach used here is somewhat similar to the approach previously used by Thomas et al.[12] and Kutler et al.[13] in their inviscid steady flow computations. Their predictor-corrector approach has been modified for the present unsteady computations.

The notation used for the "shock-fitting" procedure is shown in Fig. 5. The local velocity of the shock is given by

$$\boldsymbol{U}_s=U_s\boldsymbol{n}_s \tag{23}$$

where $\boldsymbol{n}_s$ denotes the outward unit normal to the shock given by

$$\boldsymbol{n}_s=\Big[\boldsymbol{i}_\eta-\frac{\delta_\xi}{1+K\delta}\,\boldsymbol{i}_\xi\Big]\Big/\Big[1+\Big(\frac{\delta_\xi}{1+K\delta}\Big)^2\Big]^{1/2} \tag{24}$$

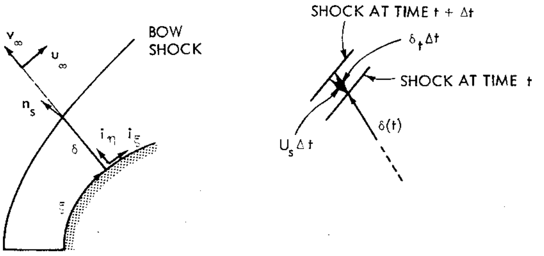

Fig. 5 Notation for "shock-fitting" procedure.

The magnitude of the local shock velocity then can be related to δ_t by

$$U_s=\delta_t\Big/\Big[1+\Big(\frac{\delta_\xi}{1+K\delta}\Big)^2\Big]^{1/2} \tag{25}$$

The vector component of the fluid velocity normal to and measured with respect to the moving shock is given by

$$\boldsymbol{V}_1=[\,(v_\infty\boldsymbol{i}_\eta+u_\infty\boldsymbol{i}_\xi-\boldsymbol{U}_s)\cdot\boldsymbol{n}_s\,]\boldsymbol{n}_s=-V_1\boldsymbol{n}_s \tag{26}$$

from which δ_t can be obtained as

$$\delta_t=V_1\Big[1+\Big(\frac{\delta_\xi}{1+K\delta}\Big)^2\Big]^{1/2}+v_\infty-u_\infty\Big(\frac{\delta_\xi}{1+K\delta}\Big) \tag{27}$$

At the beginning of the predictor step, the shock location is computed from the Euler predictor equation

$$\overline{\delta^{n+1}}=\delta^n+\Delta t\,\delta^n_t \tag{28}$$

using Eq. (27) to evaluate δ^n_t. The derivative δ^n_ξ that appears in Eq. (27) is evaluated using the second-order central difference formula:

$$\delta^n_\xi=(\delta^n_{k+1}-\delta^n_{k-1})/2\Delta y\quad(2\leq k\leq NK-1) \tag{29}$$

For the grid points immediately above and below the shock intersection point, it is not acceptable to use Eq. (29). Instead, second-order, one-sided difference formulas have been employed at these grid points.[6] For convenience, the intersection point is placed halfway between two adjacent grid points.

The pressures immediately behind the bow shock are computed using the standard MacCormack predictor, Eq. (21). Once the pressures are determined, V_1 and the remaining flow variables along $j=1$ are computed readily using exact shock jump relations.[14] This completes the predictor step. The corrector step is similar to the predictor step except that the shock standoff distance is evaluated using the modified Euler corrector:

$$\delta^{n+1}=\delta^n+\Delta t(\delta^n_t+\overline{\delta^{n+1}_t})/2 \tag{30}$$

and the pressures behind the bow shock are computed using a modified MacCormack corrector scheme in which the usual backward difference for $\partial G/\partial z$ is replaced by a forward difference.

The calculation of the boundary conditions along $j=1$ using the "shock-fitting" method described previously is performed before the predictor or corrector steps are initiated at interior grid points. All other boundary conditions are calculated after the predictor or corrector step is completed at all interior grid points. The flow conditions along the supersonic outflow boundaries ($k=1$ and $k=NK$ in Fig. 3) are determined using a second-order extrapolation of interior grid-point data. For example, the pressure along $k=NK$ are obtained from

$$p_{j,NK}=3p_{j,NK-1}-3p_{j,NK-2}+p_{j,NK-3} \tag{31}$$

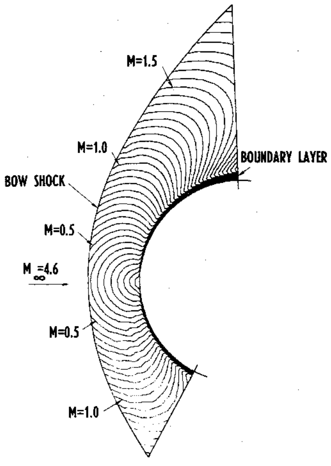

Fig. 6 Mach number contours for no shock impingement.

Along the body surface, the following conditions are imposed:

$$p_{NJ,k}=p_{NJ-1,k},\quad T_{NJ,k}=T_w \tag{32a}$$

$$\rho_{NJ,k}=p_{NJ,k}/RT_{NJ,k},\quad u_{NJ,k}=0\quad v_{NJ,k}=0 \tag{32b}$$

Initial Conditions

In all computations performed thus far, the blunt body flow without the impinging shock was computed first. The initial conditions for this calculation are obtained in the following manner. First, the approximate curve fit of Billig[15] is used to find the location (δ) and slope (δ_ξ) of the bow shock at each grid point along $j=1$. With δ and δ_ξ known and δ_t set equal to zero, Eq. (27) can be used to find V_l. Shock jump relations then can be employed to find the remaining flow variables behind the bow shock.[14]

The initial flow conditions at the wall are obtained using the known wall temperature in conjunction with pressures computed from the modified Newtonian expression

$$p_w=(p_{\text{stag}}-p_\infty)\cos^2\theta+p_\infty \tag{33}$$

where p_{stag} is computed using Rayleigh's pitot formula.[16] The initial flow conditions at interior grid points are determined by assuming a linear variation between the flow conditions immediately behind the bow shock and the wall conditions.

After a "steady-state" solution is achieved for the undisturbed blunt body flow, the impinging shock is introduced by resetting the freestream flow variables above the intersection point equal to the values that exist behind the desired oblique impinging shock. The computation then is restarted and is continued until the final "steady-state" solution is reached.

Stability

Since the present computational method is explicit, the maximum time increment (Δt) must be limited to insure stability. For inviscid flows, this limitation is expressed by the usual C.F.L. condition.[11] For the present viscous computations, the allowable time increment is computed using the empirical formula

$$\Delta t\leq\frac{1}{1+(2/Re_\Delta)}\,(\Delta t)_{\text{C.F.L.}} \tag{34}$$

where Re_Δ is the minimum mesh Reynolds number and $(\Delta t)_{\text{C.F.L.}}$ is the time increment permitted by the C.F.L. condition.

In addition to the instability that will occur if the maximum allowable time step is exceeded, an instability has been encountered near the shock intersection point. This is believed to be due to the large gradients that are present in this region. This instability has been avoided in the present study by using the fourth-order damping scheme, proposed by MacCormack,[17] in the vicinity of the intersection point.

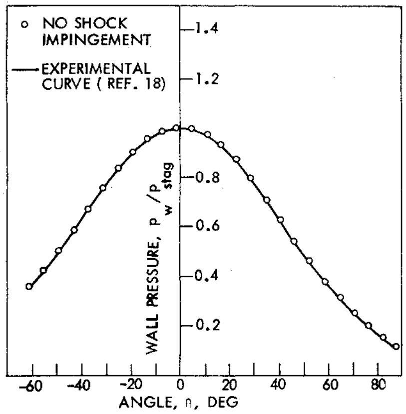

Fig. 7 Wall pressure with no shock impingement.

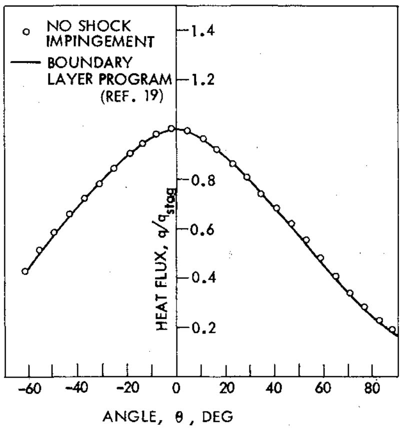

Fig. 8 Heat flux with no shock impingement.

Results

The present method has been used to compute the two-dimensional flowfields that result when various shock waves are allowed to impinge on the undisturbed flowfield surrounding a circular cylinder. The freestream conditions chosen for these computations were $M_\infty=4.6$, $Re_{D\infty}=10{,}000$, $Pr=0.72$, $p_\infty=14.93$ N/m^2, $T_\infty=167$°K, and $\gamma=1.4$, with a cylinder diameter (D) of 0.3048 m and a wall temperature of 556°K. The freestream Mach number and the angles of the impinging shock waves were chosen to correspond with the three-dimensional tests of Edney[2] in which planar shock waves were allowed to impinge on a hemisphere. Although the present computations are two-dimensional, qualitative comparisons still can be made with the Edney experiments, especially near the bow shock where the flow is locally two-dimensional.

A mesh consisting of 31 grid points in the z direction and 51 grid points in the y direction was used in all computations. The lower outflow boundary ($\xi=0$) was located along a ray 61.5° below the undisturbed stagnation streamline, whereas the upper outflow boundary ($\xi=\xi_{\max}$) was located along a ray 88.5° above the undisturbed stagnation streamline. These boundaries were chosen so that the flow passing out of each of them was supersonic, except in the boundary layer, for both the undisturbed and disturbed (shock impingement) computations. The mesh was refined near the body ($\alpha=0$) with a stretching factor (β) equal to 1.12. For this value of β, the first grid point off the body is located at 1.13% of the shock standoff distance, as compared with 3.33% for no stretching.

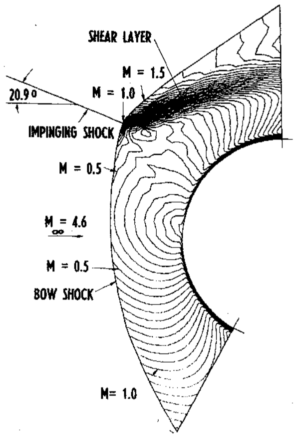

Fig. 9 Mach number contours for 20.9° shock impingement at $\theta = 36°$.

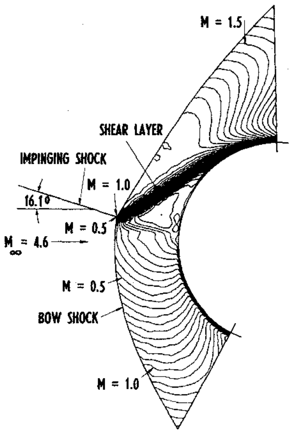

Fig. 10 Mach number contours for 16.1° shock impingement at $\theta = 9°$.

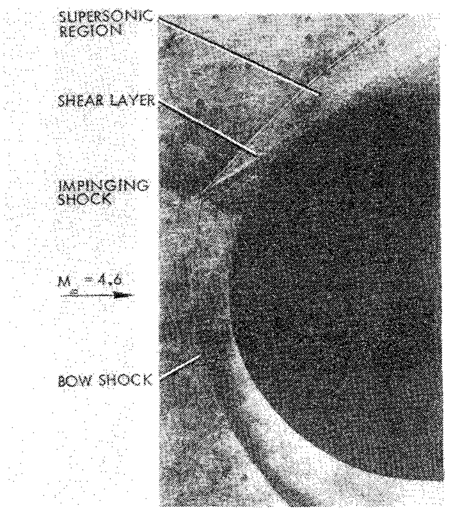

Fig. 11 Three-dimensional experimental result of Edney for 16.1° shock impingement.

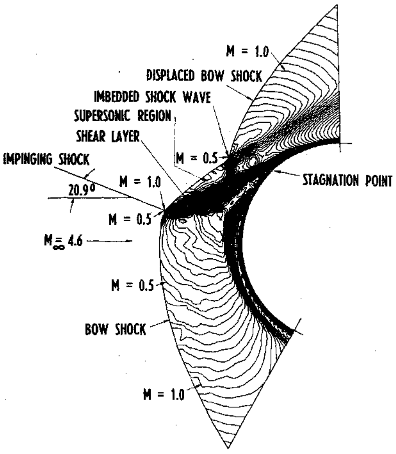

Fig. 12 Mach number contours for 20.9° shock impingement at $\theta = 9°$.

The blunt body flow without the impinging shock was computed initially. The lines of constant Mach number (contours) for this computation are shown in Fig. 6. These contour lines were drawn by a computer plotter in increments (ΔM) of 0.05 starting at $M = 0$. All other contour plots that appear in this paper were drawn in the same manner. The contours in Fig. 6 clearly show the boundary layer at the surface of the cylinder.

The wall pressures for the undisturbed calculation are compared with the experimental curve of Beckwith and Cohen[18] in Fig. 7. Excellent agreement is achieved. The heat-transfer rates for the undisturbed computation are compared in Fig. 8 with the heat-transfer rates computed by a boundary-layer program.[19] The two computations agree reasonably well, which indicates that the mesh employed in the present computations is quite adequate for resolving the boundary layer. It generally is accepted that the maximum mesh Reynolds number should be ≤ 2 to resolve all significant features of a viscous region properly. However, for the case of a boundary layer, MacCormack and Baldwin[17] have argued that, since the gradients normal to the wall are dominant, it is necessary only that the normal mesh Reynolds number be ≤ 2. In the present case, this Reynolds number ($Re_{\Delta\eta}$) is less than 2 everywhere in the boundary layer, except along the outer edge of the boundary layer near the upper outflow boundary, where a maximum value of 4.4 is reached.

Over the entire computational domain, the mesh Reynolds numbers ($Re_{\Delta\eta}$ and $Re_{\Delta\xi}$) have values that range from zero at the wall to a maximum of 290 at $j = 1$, $k = 51$. Along the stagnation streamline, the maximum mesh Reynolds number is 41 and occurs immediately behind the bow shock. As a consequence of the relatively large mesh Reynolds numbers near the bow shock, it cannot be expected that the viscous details near the bow shock will be resolved properly. This is especially true for the shock impingement cases considered next, where a shear layer emanates from the intersection point. However, in all cases the flow in the vicinity of the bow shock is predominately inviscid, so that the large mesh Reynolds numbers in this region should not alter the final results significantly at the wall.

Three cases were computed in which different shock waves were allowed to impinge on the undisturbed flowfield. In the first case, a shock wave making an angle of 20.9°, with respect to the freestream direction, was allowed to impinge on the bow shock at $\theta = 36°$ (halfway between $k = 33$ and $k = 34$ along $j = 1$). This intersection point is located just below the upper sonic line in the undisturbed flowfield. The ratio of pressures across this impinging shock wave is 2.98, and the flow deflection angle is 10°.

The Mach number contours for the resulting shock impingement flowfield are shown in Fig. 9. In this case, a shear layer emanates from the intersection point and passes out the upper outflow boundary without hitting the body. The incident shock has caused the bow shock to be moved outward a considerable distance from its undisturbed location. In addition, it causes an increase in wall pressure of 183% and an increase in heat transfer of 86% over the undisturbed values at the upper outflow boundary ($j = 31$, $k = 51$).

In the second case, a shock wave making an angle of 16.1°, with respect to the freestream direction, was allowed to impinge on the bow shock at $\theta = 9°$ (halfway between $k = 24$ and $k = 25$ along $j = 1$). The ratio of pressures across this im-

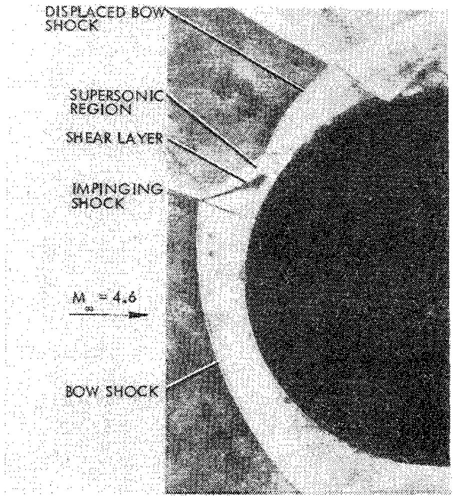

Fig. 13 Three-dimensional experimental result of Edney for 20.9° shock impingement.

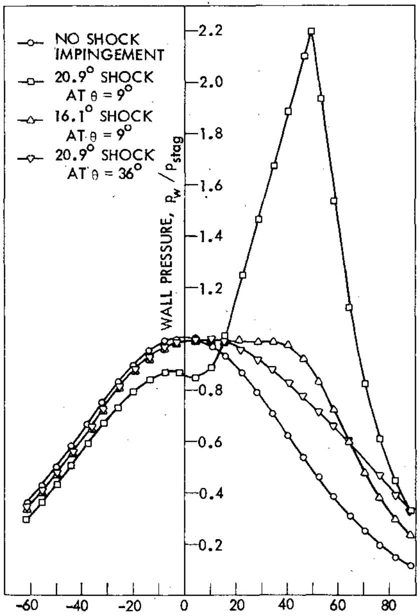

Fig. 14 Comparison of wall pressures.

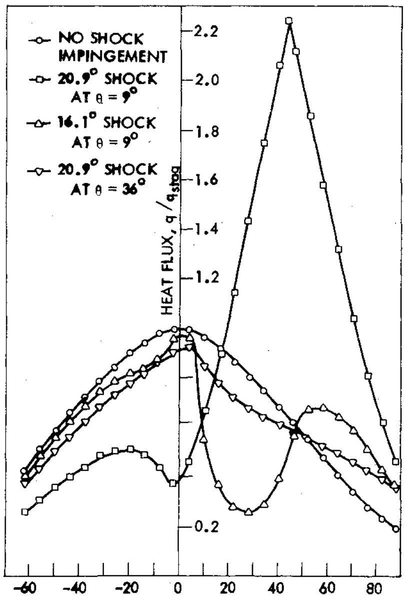

Fig. 15 Comparison of heat transfer rates.

pinging shock is 1.73, and the flow deflection angle is 5°. The Mach number contours for the resulting shock impingement flowfield are shown in Fig. 10. In this case, a shear layer emanates from the intersection point and makes a tangential approach to the body surface. This corresponds to a degenerate form of the usual Type III interference pattern, since there is no reflected shock wave from the body surface. The lack of a reflected shock wave is due to the tangential approach of the shear layer. A corresponding three-dimensional shock impingement flowfield was observed by Edney for the same shock impingement angle and a similar shock intersection location. His schlieren photograph is reproduced in Fig. 11. As a result of the impinging shock wave, the wall pressure was increased by 94%, and the heat-transfer rate was increased by 87% over the undisturbed values at the upper outflow boundary.

In the final case computed, a 20.9° shock wave was allowed to impinge on the undisturbed flowfield at the same location $(\theta = 9°)$ as in the previous computation. The resulting Mach number contours are shown in Fig. 12. The impinging shock has caused the stagnation point to be moved a considerable distance from its original location. In addition, a shear layer emanates from the intersection point and is intercepted by a shock wave that starts at the upper kink in the bow shock. Because the shear layer and the embedded shock are "captured" in the present computation, some of the detailed structure is lost, and it is difficult to determine whether this is a Type III or a Type IV shock impingement flowfield. The shock wave from the upper kink in the bow shock appears to intercept the shear layer before its hits the body, which is characteristic of a Type IV interference pattern. On the other hand, a shear layer is transmitted downstream from the upper kink in the bow shock, which is characteristic of a Type III interference pattern.

It is apparent that the contours in Fig. 12 are not as smooth as those appearing in previous figures. This is due to slight numerical oscillations, which are typical of "shock-capturing" methods. In this case, the oscillations are caused partially by the contour plotter. In subsequent computations, the oscillations have been eliminated completely by using the fourth-order smoothing scheme of MacCormack.[17] For the results shown here, smoothing was used only at mesh points in the vicinity of the intersection point.

The corresponding three-dimensional flowfield of Edney which has the same shock impingement angle as the present case and the same intersection location as before is shown in Fig. 13. This flowfield corresponds to a Type III interference pattern.

Comparisons of the pressures and heat-transfer rates on the body surface before and after impingement for all cases are shown in Figs. 14 and 15. In the present case, the impinging shock wave causes a peak pressure and peak heating rate which are both 2.2 times greater than the no-impingement stagnation point values. In addition, the bow shock has been displaced outward a considerable distance from its undisturbed location. This displacement effect is much larger in the present two-dimensional computations than is usually observed in three-dimensional experiments because the "relief" effect of the third dimension is not present here.

The results of this study were obtained on a CDC 7600 computer. About 20 min of computer time were needed for the no-impingement case, and an additional time of approximately 50 min was needed for each of the impingement cases.

Conclusions

In this study, two-dimensional shock impingement flowfields were computed using a "time-dependent," finite-difference method that solves the complete set of Navier-

Stokes equations. This method does not require prior information about the shock impingement flowfield to be computed, as is the case with previous semiempirical approaches. In addition, since the shock layer flowfield is automatically "captured" in the same manner in each computation, it is possible, in principle, to compute all six types of shock impingement with the same computer program.

The present two-dimensional results are somewhat limited in practical application because impinging shocks rarely line up perfectly with aircraft components, such as wing leading edges. In fact, the usual situation occurs when the impinging shocks cuts across the leading edge to produce a three-dimensional interaction. The significance of the present work lies in the fact that it demonstrates the feasibility of calculating the flowfield resulting from a shock wave impinging on a blunt body and that it lays the ground work for three-dimensional computations. Work is already in progress on the latter problem.[20] Although the computer demands are great, it does appear that three-dimensional computations are possible with available advanced computers.

References

[1] Hains, F. D. and Keyes, J. W., "Shock Interference Heating in Hypersonic Flows," *AIAA Journal*, Vol. 10, Nov. 1972, pp. 1441-1447.

[2] Edney, B. E., "Anomalous Heat Transfer and Pressure Distributions on Blunt Bodies at Hypersonic Speeds in the Presence of an Impinging Shock," FFA Rept. 115, Feb. 1968, The Aeronautical Research Institute of Sweden, Stockholm, Sweden.

[3] Keyes, J. W. and Hains, F. D., "Analytical and Experimental Studies of Shock Interference Heating in Hypersonic Flows," TN D-7139, May 1973, NASA.

[4] Bertin, J. J., Graumann, B. W., and Goodrich, W. D., "High Velocity and Real-Gas Effects on Weak Two-Dimensional Shock-Interaction Patterns," *Journal of Spacecraft and Rockets*, Vol. 12, March 1975, pp. 155-161.

[5] Bramlette, T. T., "Simple Technique for Predicting Type III and Type IV Shock Interference," *AIAA Journal*, Vol. 12, Aug. 1974, pp. 1151-1152.

[6] Tannehill, J. C. and Holst, T. L., "Numerical Computation of Two-Dimensional Viscous Blunt Body Flows with an Impinging Shock," NASA CR-138594, Feb. 1974.

[7] Tannehill, J. C. and Mohling, R. A., "Development of Equilibrium Air Computer Programs Suitable for Numerical Computation Using Time-Dependent or Shock-Capturing Methods," NASA, CR-2134, Sept. 1972.

[8] Tannehill, J. C. and Mugge, P. H., "Improved Curve Fits for the Thermodynamic Properties of Equilibrium Air Suitable for Numerical Computation Using Time-Dependent or Shock-Capturing Methods," NASA, CR-2470, Oct. 1974.

[9] Moretti, G. and Salas, M. D., "The Blunt Body Problem for a Viscous Rarefied Gas Flow," AIAA Paper 69-139, New York, 1969.

[10] MacCormack, R. W., "The Effect of Viscosity in Hypervelocity Impact Cratering," AIAA Paper 69-354, Cincinnati, Ohio, 1969.

[11] Tannehill, J. C., Mohling, R. A., and Rakich, J. V., "Numerical Computation of the Hypersonic Rarefied Flow rear the Sharp Leading Edge of a Flat Plate," AIAA Paper 73-200, Washington, D.C., 1973.

[12] Thomas, P. D., Vinokur, M., Bastianon, R. A., and Conti, R. J., " Numerical Solution for Three-Dimensional Inviscid Supersonic Flows," *AIAA Journal*, Vol. 10, No. 7, July 1972, pp. 887-894.

[13] Kutler, P., Reinhardt, W. A., and Warming, R. F., "Multishocked, Three-Dimensional Supersonic Flow Fields with Real Gas Effects," *AIAA Journal*, Vol. 11, No. 5, May 1973, pp. 657-664.

[14] Tannehill, J. C., Holst, T. L., and Rakich, J. V., "Numerical Computation of Two-Dimensional Viscous Blunt Body Flows with an Impinging Shock," AIAA Paper 75-154, Pasadena, Calif., 1975.

[15] Billig, F. S., "Shock-Wave Shapes Around Spherical- and Cylindrical-Nosed Bodies," *Journal of Spacecraft and Rockets*, Vol. 4, June 1967, pp. 822-823.

[16] Ames Research Staff, "Equations, Tables, and Charts for Compressible Flow," Rept. 1135, 1953, NACA, p. 7.

[17] MacCormack, R. W. and Baldwin, B. S., "A Numerical Method for Solving the Navier-Stokes Equations with Application to Shock-Boundary Layer Interactions," AIAA Paper 75-1, Pasadena, Calif. 1975.

[18] Beckwith, I. E. and Cohen, N. B., "Application of Similar Solutions to Calculation of Laminar Heat Transfer on Bodies with Yaw and Large Pressure Gradient in High-Speed Flow," NASA, TN D-625, Jan. 1961.

[19] Tong, H., "Nonequilibrium Chemistry Boundary Layer Integral Matrix Procedure, User's Manual Parts I and II," Rept. UM-73-37, April 1973, Aerotherm Corp., Mountain View, Calif.

[20] Holst, T. L., Tannehill, J. C., and Rakich, J. V., "Numerical Computation of Viscous Blunt Body Flows with a Planar Impinging Shock," *NASA Conference on Aerodynamic Analyses Requiring Advanced Computers*, March 1975, Hampton, Va.; also SP-347, NASA.